A Combined Deep Learning and Classical Potential Approach for Modeling Diffusion in UiO-66

Journal:	*Journal of Chemical Theory and Computation*
Manuscript ID	ct-2022-00010s.R2
Manuscript Type:	Article
Date Submitted by the Author:	17-May-2022
Complete List of Authors:	Achar, Siddarth; University of Pittsburgh, Computational Modeling and Simulation Wardzala, Jacob; University of Pittsburgh, Chemical Engineering Bernasconi, Leonardo; University of Pittsburgh, Center for Research Computing Zhang, Linfeng; DP Technology; AI for Science Institute Johnson, J. Karl; University of Pittsburgh, Chemical Engineering

SCHOLARONE™
Manuscripts

A Combined Deep Learning and Classical Potential Approach for Modeling Diffusion in UiO-66

Siddarth K. Achar,† Jacob J. Wardzala,‡ Leonardo Bernasconi,¶ Linfeng Zhang,§ and J. Karl Johnson*,‡

†*Computational Modeling & Simulation Program, University of Pittsburgh, Pittsburgh, Pennsylvania 15260, United States*

‡*Department of Chemical & Petroleum Engineering, University of Pittsburgh, Pittsburgh, Pennsylvania 15261, United States*

¶*Center for Research Computing and Department of Chemistry, University of Pittsburgh, Pittsburgh, Pennsylvania 15260, United States*

§*DP Technology, Beijing 100080, China; AI for Science Institute, Beijing 100080, China*

E-mail: karlj@pitt.edu

Abstract

Modeling of diffusion of adsorbates through porous materials with atomistic molecular dynamics (MD) can be a challenging task if the flexibility of the adsorbent needs to be included. This is because potentials need to be developed that accurately account for the motion of the adsorbent in response to the presence of adsorbate molecules. In this work, we show that it is possible to use accurate machine learning atomistic potentials for metal-organic frameworks in concert with classical potentials for adsorbates to accurately compute diffusivities though a hybrid potential approach. As a proof-of-concept, we have developed an accurate deep learning potential (DP) for UiO-66, a metal-organic framework, and used this DP to perform hybrid potential simulations, modeling diffusion of neon and xenon through the crystal. The adsorbate-adsorbate interactions were modeled with Lennard-Jones (LJ) potentials, the adsorbent-adsorbent interactions were described by the DP, and the adsorbent-adsorbate interactions used LJ cross-interactions. Thus, our hybrid potential allows for adsorbent-adsorbate interactions with classical potentials, but models the response of the adsorbent to the presence of the adsorbate through near-DFT accuracy DPs. This hybrid approach does not require refitting the DP for new adsorbates. We calculated self-diffusion coefficients for Ne in UiO-66 from DFT-MD, our hybrid DP/LJ approach, and from two different classical potentials for UiO-66. Our DP/LJ results are in excellent agreement with DFT-MD. We modeled diffusion of Xe in UiO-66 with DP/LJ and a classical potential. Diffusion of Xe in UiO-66 is about a factor of 30 slower than Ne, so it is not computationally feasible to compute Xe diffusion with DFT-MD. Our hybrid DP-classical potential approach can be applied to other MOFs and other adsorbates, making it possible to use an accurate DP generated from DFT simulations of an empty adsorbent in concert with existing classical potentials for adsorbates to model adsorption and diffusion within the porous material, including adsorbate-induced changes to the framework.

Introduction

Metal-organic-frameworks (MOFs) are a class of crystalline materials of great scientific and technological interest. They are highly versatile due to their permanent porosity and ability to tune pore sizes and the chemical environment of the pores.[1–5] Microporous and nanoporous materials in general possess molecular scale porous character, making them unique in comparison to other industrially relevant materials. The advantage of MOFs is the extensive customization that can be achieved using inorganic bricks or metal oxyhydroxide secondary building units (SBUs) and organic ligands (linkers) to create highly porous three-dimensional structures with high pore volumes, large surface areas, and a tailorable chemical pore environment.[3–5] Thus, in principle, there are an almost unlimited number of possible MOFs that can be designed.[6,7] This makes it possible to use MOFs in a large variety of applications, including catalysis, non-linear optics, gas separation, gas storage, and sensors.[8–18]

One important application for MOFs is the capture and destruction of toxic chemicals, such as chemical warfare agents (CWAs). Zr-based MOFs, including UiO-66, UiO-67 and their functionalized derivatives, have been studied for activity toward CWA and CWA simulant degradation.[19–31] The exceptional mechanical stability and high porosity of UiO-66 makes it a popular choice for this application.[32] However, the pores of UiO-66 are very narrow, which means transport limitations may decrease its effectiveness, since diffusion of the CWA could be much slower than the kinetics of reaction. Hence, there is a need to understand the intrinsic diffusivity of molecules in UiO-66, and the effects caused by functionalization and the presence of structural defects, like missing linkers or SBUs. Addressing these issues is part of the motivation of this work.

UiO-66 is composed of SBUs consisting of 6 Zr atoms, 4 μ_3-O atoms and 4 μ_3-OH groups coordinated by 12 benzene dicarboxylate moieties (each shared between two SBUs) $[Zr_6(\mu_3\text{-}O)_4(\mu_3\text{-}OH)_4(C_8H_4O_4)_6]$. We note that a dehydroxylated version of UiO-66 exists, which is formed by heating the material in vacuum to high temperatures to eliminate the μ_3-OH groups.[33,34] The hydroxylated form of UiO-66, which is the most suitable form of UiO-66 for use in devices exposed to the atmosphere at moderate temperatures, will be considered in this work.

Experimental characterization of materials will always be essential. However, atomistic simulations can provide information and insight that complements and elucidates experimental work. Hence, simulating the structural and dynamic properties of MOFs, including diffusion of guest molecules within MOFs, is an active and complex field of research. Density-functional theory (DFT) methods provide a highly accurate approach for modeling MOFs, including periodic calculations, which mimic large-scale behavior, and cluster repre-

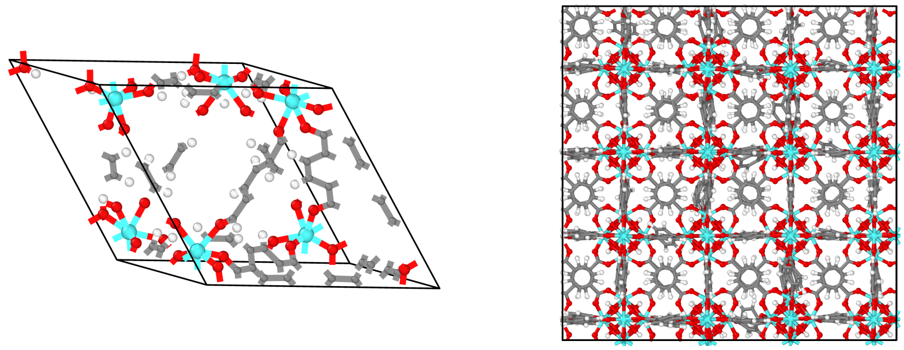

Figure 1: Left: Isometric view of a primitive cell of UiO-66. The cell contains 114 atoms: 32 O (red), 6 Zr (cyan), 28 H (white) and 48 C (grey). Right: Cubic super cell of UiO-66 containing 32 SBUs (3648 atoms). This structure was used to study diffusion of guest species in UiO-66.

sentations, which focus on the short-range local environment. Many DFT studies of MOFs have been published recently, focusing on their electronic and vibrational properties,[35,36] catalytic properties,[37–39] and adsorption capabilities.[40,41] Nevertheless, modeling MOFs using first-principles methods remains problematic, because of high computational cost and unfavorable scaling, which limits DFT studies to small system sizes (of the order of a few hundred atoms) and short time scales (typically picoseconds). These limitations are especially challenging for MOFs with large unit cells containing many hundreds to thousands of atoms. Moreover, the study of diffusion of guest molecules within MOFs via DFT is impractical for all but the smallest systems. Molecular dynamics (MD) simulations that use parameterized force fields provide a convenient means to overcome some of the limitations of DFT methods. These approaches involve fitting atomic interactions to empirical, *ab initio*, or DFT data.[42–50]

The diffusion of molecular species in MOF cavities is an important issue that has been addressed using parametrized force fields, with or without the explicit inclusion of the flexibility of the MOF framework atoms.[51–61] Although the use of rigid MOF force fields reduces the complexity of the atomic interaction model, allowing simulations of larger systems and longer times, the impact of this approximation on the description of the interactions between the MOF and the guest species has to be carefully assessed on a case-by-case basis.[19,54,61–66] Yang and Sholl[62] compared self-diffusion coefficients computed for 12 adsorbates in 17 different MOFs using both rigid and flexible models to characterize the impact of framework flexibility on diffusion. As expected, they found that for adsorbates having sizes similar to the window size, diffusion in the rigid MOFs can be orders of magnitude smaller than in flexible MOFs. However, they also found that for flexible adsorbates, e.g., n-butane, there are cases where the self-diffusion coefficient computed for a rigid MOF is orders of magnitude larger than in a flexible MOF. They found that the differences in diffusivities cannot be accurately described using the size of the pore windows, even if the flexibility of empty windows at the temperature of interest was taken into account. They conclude that the adsorbate-loaded window size was a useful descriptor for capturing the impact of framework flexibility.[62]

Generating classical force fields for MOFs that accurately account for framework flexibility is an active and important area of research. There are two broad classes of classical potentials for MOFs: (1) potentials that are derived for a specific MOF, usually based on DFT calculations, and (2) general purpose potentials, applicable to many different MOFs. The QuickFF formalism[67,68] is an example of the former class of potentials designed for specific MOFs. The original QuickFF program relied on cluster calculations,[67] but has since been extended to allow for calculations on periodic systems as input.[68] MOF-FF[46,69] is another example of a formalism for generating potentials for specific MOFs based on quantum chemical calclulations. Generalized force fields include BTW-FF,[43] ZIF-FF,[70] and UFF4MOF.[44,45] BTW-FF uses periodic MOF structures and electron density from DFT calculations to parametrize a classical potential which uses the functional form of the MM3 potential.[43] Atoms-in-molecules theory[71] is used to calculate point charges from the electron density. This method was tested for a number of Zn, Cu and Zr based MOFs in an effort to produce a transferable potential form for MOFs.[43] ZIF-FF uses an existing reference potential, and then optimizes selected parameters on the basis of periodic DFT data. In the calculations carried out with this potential, the bonded terms containing Zn were optimized to reproduce DFT calculated strain energies, while the remaining linker bonded terms were left unchanged with respect to the reference potential. ZIF-FF has been shown to predict a number of properties more accurately than the initial reference potential, across a number of ZIFs.[70] UFF4MOF is a modification of the original UFF force field,[72] extended to include transition metals, lanthanides, and additional oxygen parameters that give reliable structures for a very wide range of MOFs.[44,45]

These methods all rely on empirical functional forms to represent bonded terms and these generally do not allow for bond breaking and bond formation events. Moreover, many bonded potentials only capture the harmonic behavior of bond stretching and bending. A better approach is to directly use periodic DFT calculations covering a wide range of conditions to generate a rich training set for an efficient and highly flexible model that can be used to reproduce the chemical and physical properties of MOFs with near-DFT accuracy without resorting to fixed empirical potential forms. Machine learning (ML) offers one approach to accomplish this goal.

ML has been used for several applications related to MOFs. Zhang *et al.*[73] used recurrent neural networks with Monte Carlo to design MOFs for desired target applications. Moghadam *et al.*[74] employed neural networks to predict the mechanical properties of existing and hypothetical MOFs. Shi *et al.*[75] used an ML assisted high-throughput computational screening to identify promising MOFs for specific applications like methane storage, hydrogen storage and carbon dioxide separation. Chong *et al.*[76] have discussed the role of ML in predicting a variety of properties (gas adsorption and storage, mechanical and electrical properties *etc.*) of MOFs. They have shown how to make use of various input descriptors to store structural, positional, and chemical information. Gurnani *et al.*[77] applied a computational pipeline that involved descriptor extraction, MOF fingerprinting, and deep learning protocols to develop ML models of methane uptake using a rich methane uptake database.

None of the applications of ML to MOFs listed above involved developing atomistically detailed models that can replace the empirical MOF potentials for simulating the dynamical and structural properties of MOFs, including diffusion of guest molecules. To the best of our knowledge, only the work of Eckhoff and Behler[78] deals with the development and use of ML force fields to model the dynamical and structural properties of MOFs at an atomistic level. This paucity of atomically-detailed ML potentials for MOFs can likely be attributed to the large unit cell size and chemical complexity that characterize MOFs, compared to other periodic materials for which ML potentials have been generated.

Currently available methods for generating ML-based inter-atomic potentials include the Behler-Parrinello neural network (BPNN),[79] the deep tensor neural network (DTNN),[80] the Bonds-in-Molecules neural network method (BIM-NN),[81] the gradient domain machine learning (GDML)[82] and the Deep potential-smooth edition used in the DeePMD-kit package.[73,83–85]

We here make use of the smooth version of the DeePMD formalism,[84] which is an end-to-end symmetry preserving inter-atomic potential energy model, to construct a deep-learning potential (DP) for UiO-66. DeePMD is compatible with third-party software like the Large-scale Atomic/Molecular Massively Parallel Simulator (LAMMPS)[86] and python tools, like the atomic simulation environment (ASE),[87] making it convenient to efficiently predict a wide range of physical properties.

As stated above, the only atomistic ML potential for a MOF of which we are aware was produced by Eckhoff and Behler,[78] who used a BPNN to develop a neural network (NN) potential for MOF-5. The resulting potential was used to predict the energies, forces, and bulk properties (lattice parameters, elastic constants, bulk modulus, and negative thermal expansion coefficient) of MOF-5. They compared their predictions to DFT calculations. The approach of Eckhoff and Behler used DFT calculations of small molecular fragments to train their NN potential for periodic bulk MOF-5. This approach is generally more computationally efficient than using periodic DFT calculations to generate the training set. Indeed, for MOFs having primitive cells containing on the order of a thousand atoms carrying out periodic calculations could be be computationally prohibitive. However, the molecular fragment approach also has short-comings: (i) there is no universal way of choosing molecular fragments for all MOFs; (ii) predicted energies are sensitive to the choice of fragments. A poor choice of fragments may lead to inconsistencies in how the potential is built when periodic boundary conditions are taken into account.

Therefore, the approach we adopt in this work makes use of periodic DFT calculations on the primitive cell of UiO-66 to generate the training and testing sets for the DP. In this work we develop an optimized DP training technique that samples training data from a pool of DFT-MD simulation frames of expanded and compressed UiO-66 primitive cells. We find excellent agreement between structural properties such as bulk modulus and lattice constant predicted by our DP and those obtained from DFT calculations and experiment. We also show that our DP can predict dynamic properties, such as velocity autocorrelation functions, with higher accuracy than classical potentials, like the one developed by Rogge *et al.*[88]

The most important and interesting applications of MOFs involve the interaction of guest (adsorbate) molecules with the MOF, *e.g.*, to study diffusion and adsorption of molecules within the MOF. However, no ML potential has been developed that accounts for MOF-adsorbate interactions. In principle, framework-adsorbate interactions could be included in a straight-forward way by using DFT simulations of MOFs with adsorbates in the training set. A NN potential or DP trained in this way must include MOF-adsorbate and adsorbate-adsorbate interactions, effectively building a DP for the MOF and the adsorbate at the same time. This means that one must construct a new DP for each MOF-adsorbate pair or use a massive training set including DFT calculations with all adsorbates of interest in the MOF, including their mixtures. An alternate approach is to make use of existing classical potentials for adsorbate-adsorbate interactions, which have been shown to perform very well for predicting properties of pure fluids and mixtures.[89] Many of these empirical potentials are coarse-grained at the level of the united atom model, making them very efficient.[90–92] However, one must still include framework-adsorbate interactions. These can be tackled in the same way as classical MOF potentials, *i.e.*, through the use of combining rules to account for nonbonded atom-atom (or atom-united atom) interactions.

Our hypothesis is that we can follow a similar approach by using our DP trained on an empty MOF, a classical potential to describe adsorbate-adsorbate interactions, and combining rules to account for framework-adsorbate interactions. This is accomplished by assigning nonbonded potentials to each atom in the MOF framework, *e.g.*, from UFF[72] or DREIDING.[93] We thus use a hybrid DP-classical potential approach to carry out MD simulations of adsorbates diffusing within UiO-66. Our approach allows for adsorbates to dynamically interact with the framework, allowing the framework to respond to the adsorbate as it passes through the window. Note that Yang and Sholl identified this feature as critical to accurately accounting for the impact of framework flexibility.[62] This is in contrast to earlier methods, which used snapshots from DFT simulations of empty MOFs to estimate the diffusivities in flexible MOFs.[94] Our results provide a proof-of-concept showing the feasibility of a hybrid approach to modeling the diffusion of molecules in MOFs, with near-DFT accuracy for the description of the MOF and enhanced computational efficiency compared to *ab initio* MD approaches.

Computational methods

DFT calculations

We used the DeePMD formalism[84] to construct a DP for UiO-66. As demonstrated by Achar *et al.*,[95] DeePMD potentials trained on very small periodic cells can be used to simulate much larger supercells with high accuracy and efficiency. In this work, we therefore used the primitive cell of UiO-66 (Figure 1 left) to train the DP. The DFT-optimized cell parameters for the primitive cell are $a = b = c = 14.83$ Å and $\alpha = \beta = \gamma = 60°$.[96] The space group of UiO-66 is *Fm-3m*.[97] This cell was used for predicting structural and dynamic properties. A larger cubic super-cell consisting of 32 primitive cells (Figure 1 right) was used for studying diffusion in UiO-66 from both our DP and two empirical potentials.

The primitive cell of UiO-66 was first structurally optimized using the Vienna *ab initio* simulation package (VASP).[98–101] We employed the projector augmented-wave (PAW) method[102] to describe the electron-ion interactions. We used the generalized gradient approximation exchange-correlation functional of Perdew-Burke-Ernzerhof (PBE).[103,104] No symmetry constraints were imposed during the structural optimization. Only the Γ-point was included in the Brillouin zone sampling. We used the Methfessel-Paxton method to determine partial occupancies with a smearing width of 0.05 eV. The cutoff energy for the plane-wave basis set was set to 400 eV. The convergence criterion for electronic self-consistent loop was set to 10^{-4} eV. The convergence criterion for the ionic relaxation loop was 10^{-3} eV. The optimized structure was used to initialize the DFT-MD VASP simulations used to generate the training and testing data sets. DFT-MD simulations in the NVT ensemble were carried out using a Nosé-Hoover thermostat[105] with a frequency of temperature oscillations set to 40 time steps (SMASS = 0). We used a time step of 0.5 fs to integrate the equations of motion.

DP training

Our process for training and evaluating DPs involved creating several generations of different DPs, employing two training phases. Each DP was fitted to training sets consisting of DFT calculations on the periodic primitive cell of UiO-66. For each of the DPs generated, the training configurations were distributed among several batches and a neural network was used to predict the energies and forces using only the atomic coordinates and element types of the training configurations as input. The total energy of the system was computed as the sum of individual atomic energies. The energy of an atom i was calculated based on the number of neighboring atoms within a cut-off radius R_c.

Since the structure of UiO-66 is highly porous and the unit cell contains empty regions (pores), localizing the interaction of one atom with a small set of neighbors can reduce the generality of the potential. For this reason, we imposed a large cutoff radius of 8 Å with a smoothing cut off of 1.5 Å. The atomic coordinates from the DFT-MD simulations were used to build descriptors that contained radial and angular information about the system, to ensure translational, rotational and permutational invariance. The advantage of using the featurization in DeePMD as compared to other NN methods like BPNN is that it does not use hand-crafted local symmetry functions, eliminating the need for human intervention.[84] These descriptors were treated as input data for a three-layered feed-forward neural network. We used cylindrical NNs for the first training phase, with three layers of 340 nodes per layer. We used inverted pyramid NNs for the second training phase, with three layers (1020, 680, 340). These nodes contain a combination of linear and non-linear transformations (activation functions). Each neural network was designed to output the individual atomic energies and forces. The neural network parameters were optimized by enforcing the minimization of a loss function given by,

$$L(p_\epsilon, p_f) = \frac{p_\epsilon}{N}\Delta E^2 + \frac{p_f}{3N}|\Delta F_i|^2, \tag{1}$$

where ΔE^2 and $|\Delta F_i|^2$ denote the RMSEs of the total energies and atomic forces. Initial values of the prefactors p_ϵ and p_f were set to 0.02 and 1,000 respectively. These prefactors were automatically adjusted during training; p_ϵ was increased and p_f was decreased during the training epochs. This was done so that the force term dominates at the beginning, while the energy term dominates at the end; an approach recommended by Zhang *et al.*[83] The training of the neural network was carried out for a total of 10^6 batches to achieve higher accuracy and avoid overfitting. More details about the training hyperparameters used for DeePMD are provided in the Supporting Information.

As noted above, we used two training phases to obtain the final DP for UiO-66. The first phase consisted of an iterative training approach where each DP generated was evaluated based on its ability to predict the energy-volume response, *i.e.*, the equation of state, of UiO-66. A schematic representation of the first training phase is shown in Figure 2. The use of an energy-volume response criterion guarantees that the DP accurately accounts for the mechanical properties of UiO-66 under both expansion and compression. Once we obtained a DP that was able to predict the equation of state with acceptable accuracy, we used that DP as the starting point for the second training phase. The second training phase was designed to explore framework flexibility by adding training data generated from high temperature DFT-MD simulations and active learning.

For the first phase of training, we sampled a number of expanded and compressed primitive cells of UiO-66. The atomic positions for each of these samples were optimized with the same convergence criteria adopted for the equilibrium lattice. A base training set was generated using the relaxed equilibrium lattice cell from an NVT simulation carried out at $T = 600$ K for 5 ps (a total of 10,000 MD steps). The validity of the DP obtained from a set of atomic configurations was assessed using the root mean squared errors (RMSE) of predicted energy per atom *vs.* volume data not included in the fitting of the DP. The test data included the energy *vs.* volume response computed from VASP by considering expansion and compression of the cell parameters within a range of $\pm 6\%$ with respect to the equilibrium parameters. We set an arbitrary target RMSE value of 10^{-3} eV per atom for predicting the entire set of expanded and compressed DFT configurations. If the RMSE for a given DP was found to be larger than this value, additional expanded and compressed configurations were included in the training. The details of this process are discussed below.

The final set of data generated in the first phase was used as the starting dataset for the second phase of training. As stated above, the second phase was designed to improve the ability of the DP to capture framework flexibility. We therefore added configurations from NVT DFT-MD simulations at $T = 1,000$ K and $T = 1,200$ K. To further ensure that the training data explored a significant part of the potential energy surface, we used the deep generator (DP-GEN) package by Zhang *et al.*[107] The DP-GEN scheme is designed to produce accurate DPs using active learning and is distributed through the Deep Modeling software ecosystem.[106] This scheme uses successive iterations composed of exploration, labeling, and training. The exploration step involves sampling of configuration space and transferring

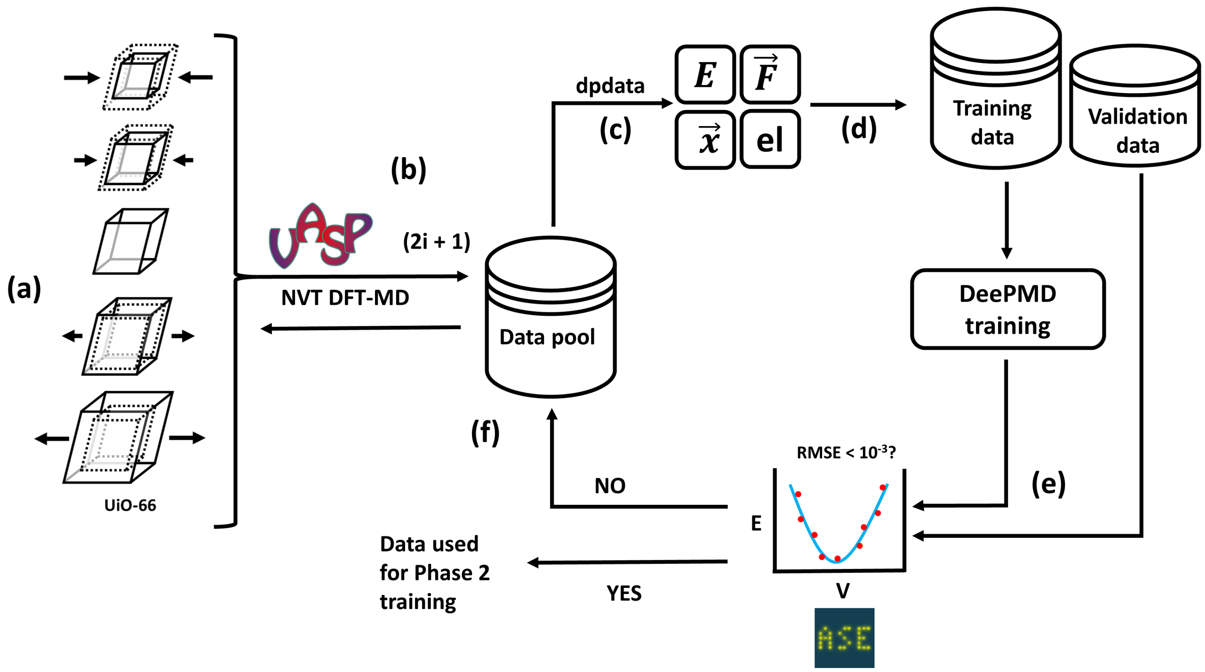

Figure 2: Schematic representation of the first training phase used to generate a DP for UiO-66. (a) Atom positions in the equilibrium, compressed, and expanded primitive cells were first relaxed at iteration i. (b) Selected relaxed structures were then used as starting configurations for VASP NVT DFT-MD simulations; the output of the simulations were stored in a data pool. (c) At a given iteration, energies, forces, atomic coordinates and their element types were extracted using dpdata (from the deepmodeling package[106]) from the data pool. (d) The extracted information was then used as data for training. (e) A trained DP was obtained and its quality assessed based on the convergence of the energies as a function of volume relative to VASP results. If the RMSE was below the predefined tolerance, the DP training was considered complete. (f) If the RMSE was above the tolerance, the training dataset was further expanded with additional NVT-MD simulation configurations for compressed and expanded cells. Once converged, the final dataset was used for training DPs in the second phase.

these configurations to the labeling step. An ensemble of DPs is generated by training from a single training set but with a difference in the initialization of the model parameters (weights). Different parameter initialization can lead to training different potential energy surfaces. With sufficient training data, the ensemble of DPs should all correspond to similar potential energy surfaces and thus produce predictions that are close to each other.

In our implementation of DP-GEN we trained an ensemble of 4 DPs (DP-0 to DP-3). We then performed DP-MD simulation for 50 ps using DP-0 from the ensemble. An error indicator was generated by using the configurations from the DP-MD run to evaluate the forces computed from each of the other members of the DP ensemble. The error indicator is defined as the maximal standard deviation of the atomic forces predicted from the ensemble of DPs. We then define upper and lower bound of this maximal standard deviation of forces for each iteration. Configurations with maximal force deviations that fall within these bounds will then be re-labeled using single-point DFT calculations and added to the training dataset. This re-labeled dataset is then used to train the DPs as part of the training step for a given iteration. These newly trained models are further used to generate and explore larger configuration space as part of the next iteration. More details on the workings of DP-GEN are reported by Zhang *et al.*[107]

Classical potentials

We used classical potentials for UiO-66 to compare with results from our DP calculations. The dynamic properties of the empty MOF were computed with the Rogge *et al.* potential.[88] The atomic charges in this potential were calculated using the minimal basis iterative stockholder partitioning scheme,[108] while covalent parameters were developed using QuickFF.[67] The atomic point charges were replaced by Gaussian functions centered on each respective atom. We computed diffusion of Ne in UiO-66 with both the Rogge *et al.* potential and the UFF based potential of Boyd *et al.*,[109] combined with atomic point charges found from electron density calculations using the DDEC6 approach.[63] The Rogge *et al.* potential was shown to give a more robust and physical representation of UiO-66 than the UFF based Boyd *et al.* potential.[63] Moreover, guest-MOF binding energies were estimated and found to be in excellent agreement with *ab initio* results.[63]

Results and discussion

DP training and validation

We first discuss the validation of the DPs that were generated in the first training phase shown in Fig. 2. DPs at each iteration ($i = 0, 1, ...$) in the first phase of training were obtained by standard training to the loss function, eq. 1. Then, the DP was validated by comparison with the energy *vs.* volume dependence obtained with VASP. These results are plotted as individual energy *vs.* volume diagrams in Figure 3. Each version of DP used the same neural network architecture as described in the methods section, with varying training samples. For Figure 3 the light green circles are the starting configurations of the NVT DFT-MD simulations from which the DPs were trained. We label individual DP versions "DP-v$_i$". DP-v$_0$ (Figure 3a) was trained using a base training set consisting of 10,000 DFT-MD configurations with the equilibrium cell parameters of UiO-66. The RMSE in energy per atom calculated for this base DP was 8.5×10^{-3} eV/atom, which was well above the preset threshold of 10^{-3} eV/atom. DP-v$_1$ was therefore generated using 3 sets of DFT-MD training data ($2i+1$). Two of the three DFT-MD simulations (the left and right green circles in Figure 3b) used a crystal cell whose lattice constants were reduced by 2.5% and increased by 2.5%, respectively. These structures were optimized with VASP and DFT-MD simulations of 0.5 ps (1,000 steps long) were run for each starting configuration. Thus, DP-v$_1$ was trained using a total of 12,000 atomic configurations. The RMSE in energy per atom calculated for DP-v$_1$ was found to be 2.4×10^{-3} eV/atom, which was still above the acceptable threshold. A new potential, DP-v$_2$, was generated next, using additional NVT DFT-MD simulation data with different starting configurations. From Figure 3c, the leftmost and the rightmost training samples had lattice constants that were reduced by 5% and increased by 5%, respectively. This resulted in a total of 14,000 training configurations. The RMSE in energy per atom calculated for this potential was 7.2×10^{-4} eV/atom, which was below the 10^{-3} eV/atom threshold. Thus, DP-v_2 was adopted as the final DP from the first phase training and no further iterations were run. Figure 3d summarizes the trend in RMSE for each version of DP, and it shows that the quality of each subsequent version improves with additional training data. More details are provided in the Supporting Information.

For the second phase of training, we started with the DP-v_2 dataset and pruned it to reduce redundant configurations that were correlated and to reduce the training time. We validated that pruning the dataset did not lead to a decrease in energy *vs.* volume prediction accuracy of our DP. High temperature DFT-MD simulations at $T = 1,000$ K and $T = 1200$ K composed of 2,000 configurations each from 5 ps long simulations were added to the dataset. This dataset was used for the first iteration of active learning using DP-GEN. During the first DP-GEN iteration, we identified 1,000 additional configurations for re-labeling. We then ran a second iteration of DP-GEN with the new dataset that included single-point DFT calculations of the re-labeled data. The final dataset consisted of 7,800 configurations from a diverse set of calculations. The final DP was taken from the second DP-GEN iteration. Details of this procedure are given in the Supporting Information.

Energy and force prediction

It is critical to perform a validation of the potential; we did this by evaluating the predicted atomic forces and total energies of UiO-66 for unseen configurations. We used a total of 6,000 testing configurations from four different DFT-MD simulations. Each simulation used the five final configurations from the DFT-MD simulations used for training this DP (as in Figure 3c) as the starting point for each set of 5 ps (10,000 steps) DFT-MD simulations. The simulations were performed at different temperatures, $T = 350, 600,$ and $1,000$ K. The test data frames were collected every 50 steps from each simulation, for a total of 6,000

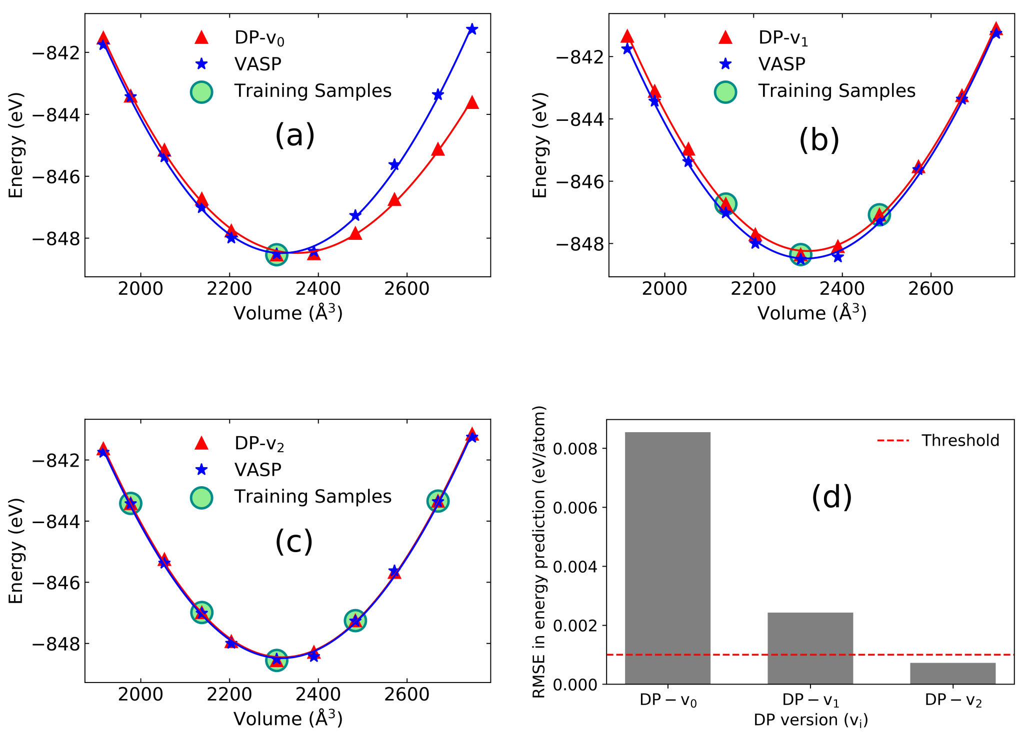

Figure 3: Energy *vs.* volume dependence prediction for different versions (v_i) of DP (red triangles), in which each version uses training samples with different volumes (light green circles). The predictions of the DPs are compared to their corresponding VASP results (blue stars). (a) DP-v_0 has an RMSE of 8.5×10^{-3} eV/atom. (b) DP-v_1 has an RMSE of 2.4×10^{-3} eV/atom. (c) DP-v_2 has an RMSE of 7.2×10^{-4} eV/atom. The blue and red lines are the Birch-Murnaghan[110,111] equation of state fits for the VASP and DP data, respectively. (d) A bar plot comparing the RMSE from these three versions of the DP and a dashed red line representing the threshold (10^{-3} eV/atom) at which a DP is considered acceptable.

configurations. Testing the DP using configurations from much longer simulation times is essential to assess the robustness of the DP. The results are shown as a parity plot in Figure 4a, where we compare the energies per atom from VASP and DP. The RMSE of the prediction was found to be 9.76×10^{-4} eV/atom.

We also computed RMS errors in atomic forces from these testing data. We show in Figure 4b a parity plot of the forces predicted by DP and those computed with VASP. The forces in the three spatial directions (x, y and z) are plotted in the same figure. The RMSE calculated for the force prediction was found to be 0.055 eV/Å. Compared to the results reported by Eckhoff and Behler,[78] we obtain better accuracy in our predicted RMSE values. For the periodic bulk structures of MOF-5, Eckhoff and Behler[78] achieved an RMSE of 6.5×10^{-3} eV/atom for energies and 0.13 eV/Å for forces. It is important to note that this comparison is based on two different types of neural network potentials and two different MOF structures. We therefore cannot definitively ascribe the increase in accuracy of our DP relative to that of Eckhoff and Behler to our use of periodic DFT in the training sets.

Predicting structural characteristics of UiO-66

We have used our DP to predict the mechanical properties of UiO-66. The bulk modulus and the equilibrium lattice constant for the primitive cell of UiO-66 can be derived by fitting the energy-volume data to an equation of state. We calculated these structural properties from the Birch-Murnaghan (B-M) equation of state[110,111] given by,

$$E(V) = E_0 + \frac{9V_0K}{16}\left\{\left[(V_0/V)^{\frac{2}{3}} - 1\right]^3 K' + \left[(V_0/V)^{\frac{2}{3}} - 1\right]^2 \left[6 - 4(V_0/V)^{\frac{2}{3}}\right]\right\} \qquad (2)$$

where $E(V)$ is the internal energy for the cell volume V, E_0 is the internal energy at the equilibrium volume V_0, K is the bulk modulus, and K' is the first derivative of the bulk modulus with respect to the pressure. Fitting of the B-M equation was carried out using ASE.[87] The blue and red lines in Figure 3c are the B-M fits using the VASP and DP-v_2

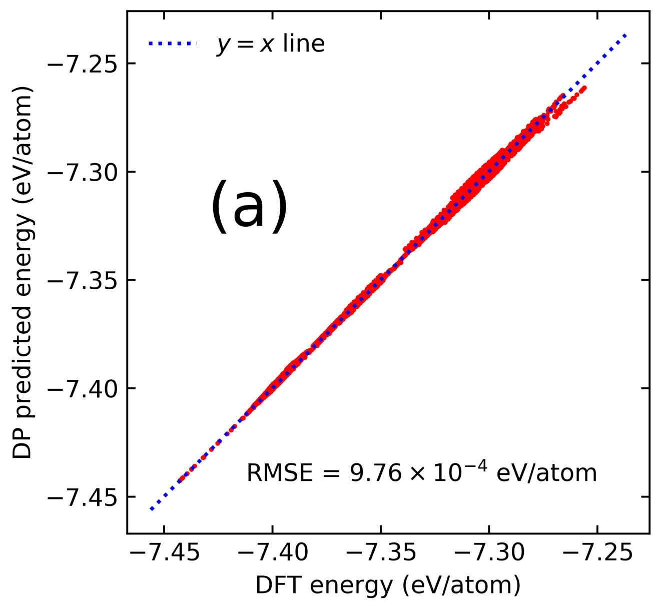

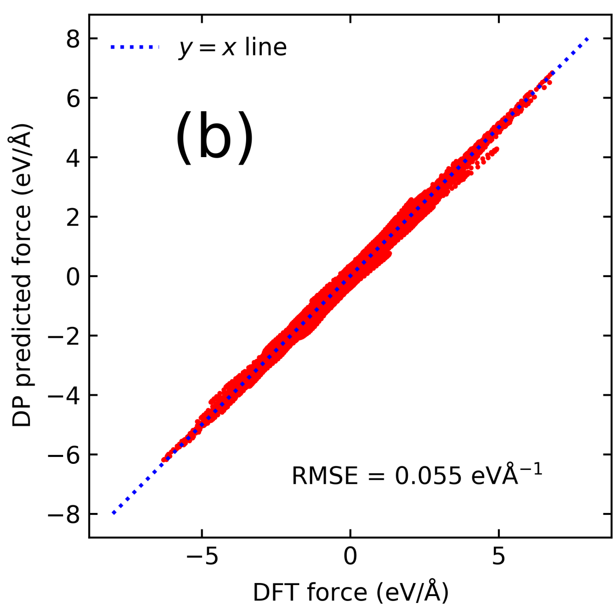

Figure 4: Parity plots of DP predicted (a) energies and (b) forces, compared with values computed from DFT. The RMSE in prediction for energies is 9.76×10^{-4} eV/atom and that for the forces is 0.055 eV/Å . Test data sets were sampled from NVT VASP simulations at $T = 600$ K.

results, respectively. The B-M fits using the final DP visually looked the same as the red line in Figure 3c. The RMSE in energy per atom *vs.* volume calculated for the final DP was slightly above that of DP-v$_2$ with a value of 9.2×10^{-4} eV/atom while still being under the threshold of 10^{-3} eV/atom. The agreement between the bulk modulus computed from DP (31.88 GPa) and from VASP (32.11 GPa) is excellent. An experimental value for bulk modulus of 37.90 GPa for UiO-66 has been reported by Redfern *et al.*[112] The VASP (PBE) bulk modulus prediction has an error of 15% relative to the value reported by Redfern *et al.* The difference could be due to either experimental limitations in characterizing bulk properties of MOFs (as reported by Redfern *et al.*) or due to inaccuracies in the level of DFT theory we used for our calculations. The bulk modulus prediction error from DP is similar to that of VASP since the DP was trained using VASP data. We also performed similar equation of state calculations for the cubic supercell of UiO-66 at 0 K using the classical potential of Rogge *et al.*,[88] as implemented in LAMMPS. A plot of the B-M fit is shown in Figure S6. This potential yields a bulk modulus of 16.37 GPa, which is significantly lower than the experimental value and values predicted by DP or DFT. A possible reason for the differences observed using the potential of Rogge *et al.* and DP can be related to the DFT approximations used in the parameterization of the force field. For the former, isolated cluster models were used in the parametrization, whose structure was optimized using the B3LYP exchange-correlation functional,[113,114] as implemented in Gaussian 09.[115] By contrast, our DP for UiO-66 was constructed with DFT data generated using the PBE functional in VASP using fully periodic MOF structures.

We calculated the equilibrium lattice constant of a conventional cubic cell (a^c) from the calculated volume of the elementary primitive cell,

$$a^c = (4V_0)^{\frac{1}{3}}. \tag{3}$$

Our DP yields a value of $a^c = 21.012$ Å, which is in good agreement with the experimental value of 20.755 Å,[116] and the value from our VASP calculations of 21.008 Å. The Rogge *et al.* potential gives a lattice constant constant of 21.463 Å.

We examined the influence of semi-empirical dispersion corrections in the DFT calculations by using the D3 correction of Grimme *et al.* with Becke-Johnson damping[117] (PBE-D3). This gave rise to a reduction of roughly 4.2% in V_0 and a reduction of 0.3% in the bulk modulus, K. Details are provided in the Supporting Information. The good agreement between PBE and PBE-D3 results indicate that the properties of empty UiO-66 are dominated by short-ranged bonded interactions rather than long-range dispersion forces.

Dynamic Properties: Velocity autocorrelation function

In this section we describe dynamic properties computed from DFT (VASP), DP, and the Rogge *et al.* potential. We computed the velocity autocorrelation function (VACF) from NVT MD simulations at $T = 350$ K for UiO-66. The system was thermally equilibrated at 350 K with a Nosé-Hoover thermostat for 3 ps and the VACF was then calculated over 0.5 ps from an NVT production run. We used the primitive cell of UiO-66 for calculations with VASP. The VACF was computed with DP using both a primitive cell and a cubic $2 \times 2 \times 2$ supercell. We computed the VACF from the Rogge *et al.* potential only with the cubic $2 \times 2 \times 2$ supercell. The VACFs computed with DP for the primitive cell and the cubic supercell were found to be virtually identical. The results are plotted as a function of the autocorrelation length in Figure 5. We observe that DP predicts a VACF that is in good agreement with the VASP VACF. The VACF computed using the Rogge *et al.* potential, on the other hand, exhibits larger deviations in amplitudes and peak locations from the VASP VACF compared with DP. It appears that the VACF computed from the Rogge *et al.* potential goes out of phase with the VASP results around 0.08 ps. The differences in the VACF computed from the Rogge *et al.* potential and VASP may be due to the cluster-based approach used in developing the Rogge *et al.* potential. The VACFs from 0.3 to 0.5 ps are plotted in Figure S8. We see from this figure that the VACFs from VASP and DP remain nearly in phase over the entire 0.5 ps range, although the amplitudes from DP are generally larger than those from VASP. The VACFs decay to zero at about 0.5 ps for all three calculations.

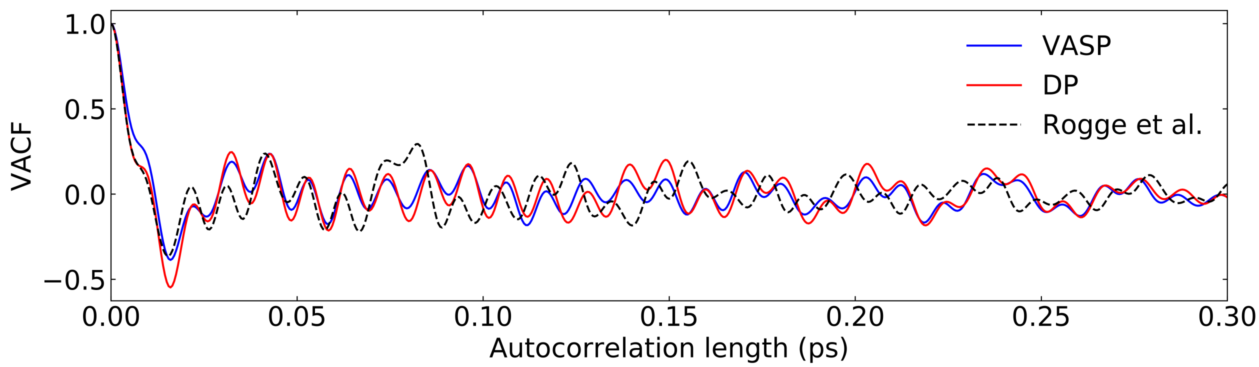

Figure 5: The velocity autocorrelation function at 350 K for UiO-66 computed from VASP, DP, and the potential of Rogge *et al.*[88] as a function of the autocorrelation length.

Diffusion of Ne and Xe in UiO-66

In this section we present results for diffusion calculations using a hybrid DP-classical potential approach to describing the framework-adsorbate interactions. We simulated diffusion of Ne as a test case because the mobility is fast enough to allow accurate diffusion calculations from DFT-MD. Moreover, although the diameter of Ne is small compared with the window size of UiO-66, Wardzala et al. showed that the self-diffusion coefficient of Ne in rigid UiO-66 is significantly slower than in flexible UiO-66.[63] We also computed diffusivity of Xe in UiO-66 because the Xe atom is much larger in diameter than Ne. We know from classical simulations that the self-diffusion coefficient of Xe in UiO-66 is almost 30 times smaller than that of Ne, due to a much larger barrier to diffusion (*vide infra*). This increased barrier is due to steric interactions between Xe and the UiO-66 pore window, as illustrated in Figure S10 of the Supporting Information. The slower diffusivity of Xe in UiO-66 prevents us from obtaining reliable estimates using DFT-MD simulations. We use the DP, trained only for C, H, O and Zr atoms within the MOF, to account for the intra-framework forces and energies.

The Ne-Ne and the Xe-Xe interactions were modeled with the Lennard-Jones (LJ) potential,

$$u_{ij} = 4\epsilon_{ij}\left[\left(\frac{\sigma_{ij}}{r_{ij}}\right)^{12} - \left(\frac{\sigma_{ij}}{r_{ij}}\right)^{6}\right], \tag{4}$$

where u_{ij} is the potential, ϵ_{ij} is the potential well depth, σ_{ij} is the diameter, and r_{ij} is the distance between a pair of LJ atoms of type i and j. The framework-adsorbate interactions were computed by assigning LJ parameters for each atom in the framework from UFF[72] and then using the Lorentz-Berthelot combining rules,

$$\epsilon_{ij} = \sqrt{\epsilon_i \epsilon_j}, \tag{5}$$

$$\sigma_{ij} = \frac{1}{2}(\sigma_i + \sigma_j), \tag{6}$$

to compute the framework-adsorbate interactions. The LJ parameters for the hybrid DP-classical calculations are given in Table 1.

Table 1: Values for the LJ parameters for the various elements in the system. The Ne and Xe parameters were taken from the literature.[118,119] The other parameters were taken from UFF.[72]

Atom	ϵ (kcal/mol)	σ (Å)
Ne	0.073	2.79
Xe	0.438	4.10
C	0.105	3.43
O	0.06	3.12
H	0.044	2.57
Zr	0.069	2.78

We performed finite loading simulations of Ne diffusing within UiO-66 using our hybrid DP-classical potential, which we denote as DP/LJ. For comparison, we performed diffusion calculations using DFT-MD at the PBE-D3 level of theory, and also using the two classical UiO-66 potentials: the Rogge *et al.* potential,[88] which we denote as Classical Potential 1/LJ (CP1/LJ), and the UFF Boyd *et al.* potential,[109] denoted as Classical Potential 2/LJ (CP2/LJ). The reason for using PBE-D3 for the DFT-MD Ne diffusion calculations is that the Ne-framework interactions are dominated by dispersion forces. We also performed zero loading Ne diffusion simulations with DP/LJ and CP1/LJ as a function of temperature in order to calculate the diffusion activation energies.

We used a version of LAMMPS locally modified to include DP in addition to standard pair potentials in MD simulations. A cutoff of 15 Å was imposed on all classical LJ interactions. Sample LAMMPS input files are provided in the Supporting Information.

MD simulations of Ne diffusion in UiO-66 were carried out with LAMMPS for the three potentials: DP/LJ, CP1/LJ, and CP2/LJ. We used a composite system consisting of the periodic cubic $2 \times 2 \times 2$ supercell of UiO-66 (32 primitive cells, see Figure 1 right) and 160 Ne atoms. This corresponds to 5 Ne atoms per primitive cell, which is the average absolute loading at an external pressure of about 100 bar at 300 K, as computed from our grand canonical Monte Carlo simulations using the RASPA software package.[120] See Supporting Information for details. Multiple independent runs (at least 5) were used to achieve satisfactory statistics. The system was equilibrated for 50 ps in the canonical (NVT) ensemble using a Nosé-Hoover thermostat[105] at 300 K. Data were then collected from long (up to 25 ns) microcanonical (NVE) simulations for the classical potentials. Use of the microcanonical ensemble eliminates the possibility of thermostat bias in the dynamics. We compared results from NVT and NVE production runs and found no impact of the thermostat on the dynamics (see Supporting Information). Therefore, DP/LJ simulations were carried out in the NVT ensemble. Since it was impractical to run DFT-MD on such large systems, we used the primitive cell of UiO-66 (Figure 1 Left) with 5 Ne atoms added for our VASP PBE-D3 diffusion calculations. The DFT-MD systems were first thermally equilibrated at 300 K for 0.1 ps in the NVT ensemble using the Andersen thermostat[121] with a collision probability of 0.75 (to generate randomized starting points for independent runs), followed by an additional equilibration for 0.5 ps using a Nosé-Hoover thermostat at the same temperature. We continued the NVT simulation with the Nosé-Hoover thermostat for the production run for 20 ps. A total of 40 independent runs were used to due to the shorter simulation times and smaller system size in the DFT-MD calculations. We used multiple time origins to calculate mean-squared displacement (MSD). For each simulation, self-diffusivities (D_S) were calculated from the production runs using Einstein's relation,

$$D_S = \frac{1}{2td}\langle \sum |r_i(t) - r_i(0)|^2 \rangle \tag{7}$$

where t is the time, $d = 3$ is the dimensionality of the system, r_i is the position of the i^{th} Ne atom at time t and the sum is over all diffusing atoms. Diffusion coefficients from the four different types of calculations are compared in Table 2. The value of D_S from each simulation was calculated by analyzing the final third of the MD simulation run to ensure that the MSD data were in the linear regime. The uncertainties in the values of D_S were computed as twice the standard deviation of the independent values. In order to estimate system size effects, we computed D_S using DP/LJ with a single primitive cell as well as the $2 \times 2 \times 2$ cubic supercell. We see that D_S increases by about 13.4% as the system size increases from 1 to 32 primitive cells. The PBE-D3 and DP/LJ results both computed for a single primitive cell agree within the estimated uncertainties of the simulations, although the uncertainties are large because of the small system sizes involved. We note that the properties of Ne computed from PBE-D3 and its interactions with the framework at that level of theory are not expected to exactly correspond to the hybrid DP/LJ approach. Nevertheless, the agreement between DFT-MD and DP/LJ-MD provides a proof-of-principle that the hybrid approach is able to accurately reproduce DFT diffusion results at a very small fraction of the cost. The times required for 1 MD time step for PBE-D3 and DP/LJ were 2,765 and 0.0083 core-seconds, respectively. The DFT calculations were carried out on two Xeon E5 nodes (56 total cores) and DP/LJ simulations were performed on NVIDIA A100 GPUs. While this speed-up of over 300,000 is significant, it is more important to note that the DP/LJ simulations scale linearly with system size, making it possible to carry out simulations 32 times larger with reasonable computational effort, while DFT calculations on a system of that size are infeasible.

Table 2: Diffusion coefficients of neon in UiO-66 at 300 K at a loading of 5 Ne per primitive cell computed from VASP (PBE-D3), hybrid DP (DP/LJ), Rogge *et al.* (CP1/LJ), and Boyd *et al.* (CP2/LJ). Cells is the system size in terms of the number of primitive cells.

Method	$D_S \times 10^8$ (m^2/s)	Cells
PBE-D3	1.52 ± 0.58	1
DP/LJ	1.49 ± 0.48	1
DP/LJ	1.69 ± 0.15	32
CP1/LJ	2.10 ± 0.09	32
CP2/LJ	1.71 ± 0.14	32

Diffusion through porous materials is typically an activated process and the activation energy for diffusion is a quantity of fundamental interest. Knowledge of the activation energy for diffusion allows one to estimate the diffusion coefficient at any (reasonably close) temperature. The diffusion activation energy can be estimated from the Arrhenius equation,

$$D = D_0 e^{-\frac{E_A}{RT}}, \tag{8}$$

where E_A may be calculated from the slope of a plot of $\ln(D_S)$ vs. $1/T$, as in Figure 6. This approach requires that D_S be computed for at least three different temperatures (to obtain statistically meaningful results) and is therefore computationally prohibitive for DFT-MD, but easily achievable for DP/LJ and classical potentials. We computed E_A for Ne in UiO-66 at zero loading from DP/LJ and CP1/LJ. We used the periodic cubic UiO-66 supercell loaded with 500 noninteracting (*i.e.,* zero loading) Ne atoms. The Ne-Ne interactions were explicitly excluded in these simulations, with Ne-framework and framework-framework interactions included in the same way as in the finite-loading simulations. The same workflow (equilibration, simulation times, *etc.*) used for the finite-loading simulations was used for the zero loading simulations. A sample input file is provided in the Supporting Information. We examined three different thermostat temperatures: 300, 350 and 400 K. The diffusion coefficients from these simulations are reported in Table 3 and the fits to the Arrhenius equation are shown in Figure 6. The value of E_A for DP is 2.91 ± 0.26 kJ/mol, which is in agreement with the prediction obtained from analogous simulations carried out using CP1/LJ (2.85 ± 0.65 kJ/mol). We would expect CP2/LJ to predict a value of E_A similar to that of the DP/LJ and the CP1/LJ potentials based on the results of finite-loading calculations.

Table 3: Diffusion coefficients, $D_S \times 10^8$, (m^2/s) for Ne in UiO-66 at zero loading computed from CP1/LJ and DP/LJ.

T (K)	CP1/LJ	DP/LJ
300	2.12 ± 0.12	2.07 ± 0.04
350	2.43 ± 0.15	2.44 ± 0.11
400	2.83 ± 0.16	2.78 ± 0.07

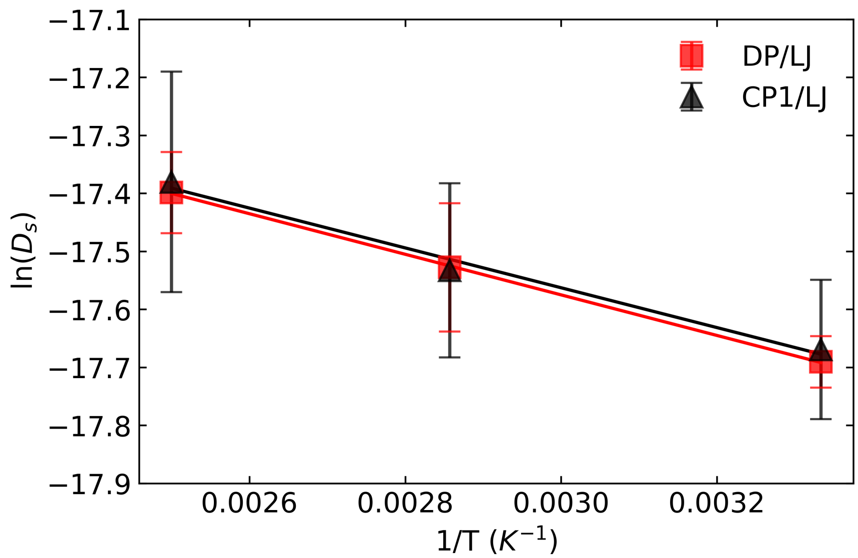

Figure 6: Arrhenius plot of diffusion coefficients for Ne in flexible UiO-66 using DP/LJ and CP1/LJ.

Diffusion of Ne within UiO-66 is not a stringent test of the ability of our DP to model framework flexibility as Ne has a very small van der Waals radius. We therefore carried out simulations of Xe diffusion in UiO-66, since Xe is much larger than Ne and is a logical choice, given that both are noble gases, having the same types of interactions with the framework. We computed diffusivities of Xe in UiO-66 with DP/LJ and CP1/LJ using the $2 \times 2 \times 2$ supercell of UiO-66 and 100 Xe atoms, excluding Xe-Xe interactions to model zero loading. We chose to simulate zero loading conditions to focus on adsorbate-adsorbent interactions, without the complications due to adsorbate-adsorbate interactions. The system was first equilibrated for 50 ps in the canonical ensemble at 400 K. We used long (25 ns) microcanonical simulations for CP1/LJ and canonical simulations at 400 K of 1 ns for DP/LJ to generate production data. We used a total of 10 independent simulations for CP1/LJ and 25 independent simulations for DP/LJ to calculate the self-diffusivity of Xe. Diffusion coefficients from the two potentials are compared in Table 4. We see that the D_S computed from DP/LJ is slightly larger than that computed from CP1/LJ. Although the values agree within the combined uncertainties, we believe that the difference between these estimates is significant and is related to the different flexibility of the linkers described by DP and CP1, and that the DP description of the linker flexibility is more realistic.

Table 4: Diffusion coefficients of xenon in UiO-66 at 400 K at zero loading computed from hybrid DP (DP/LJ) and the classical potential of Rogge *et al.*[88] (CP1/LJ).

Method	$D_S \times 10^9$ (m^2/s)
DP/LJ	1.31 ± 0.27
CP1/LJ	0.997 ± 0.16

Conclusions

We have generated the first neural network atomistic potential for UiO-66, using the DeePMD formalism. The DP was generated using a training technique that iteratively explored compressed and expanded starting structures and employed DFT-MD simulations at high temperatures and active learning. The DP generated using our technique is capable of accurately predicting the cell parameters, bulk modulus and VACF of UiO-66. We have demonstrated how this DP can be interfaced with classical force fields to simulate MOFs loaded with guest molecules without the need to generate a new DP for each new adsorbate. This hybrid approach of combining a DP with classical pairwise empirical potentials provides an efficient path for producing highly accurate potentials for pristine and defective MOFs based on relatively small DFT training sets and using these potentials to explore properties of MOFs containing a variety of guest molecules. This approach is useful for studying phenomena such as adsorption, diffusion, and loading-dependent thermal conductivity. However, it may not necessarily be suitable for modeling chemical reactions involving the MOF host and guest molecules. We showed that our hybrid DP/LJ potential predicts a diffusion coefficient for Ne in UiO-66 in excellent agreement with DFT-MD simulations, at a very small fraction of the DFT-MD computational cost. More importantly, the DP/LJ approach allows calculations with system sizes containing many thousands of atoms, which cannot be carried out efficiently using standard DFT methods. We also computed the self-diffusion coefficient for Xe in UiO-66 and we estimated a diffusivity that is more than one order of magnitude lower than Ne, indicating significant steric hindrance for Xe traversing the pore windows. Finally, we note that our DP could be trained to include bond-breaking and bond-forming events within the MOF creating open metal sites that can spontaneously form when a linker-SBU metal-oxygen bond breaks. The description of these phenomena may however require a much more extensive set of configurations for the DP training and is beyond the scope of this work.

Acknowledgement

This research was partially sponsored by the National Science Foundations (NSF) under Award No. CBET 1703266 and by the Army Research Office under Cooperative Agreement W911NF-19-2-0187. Computations were performed at the University of Pittsburgh's Center for Research Computing, and on the Extreme Science and Engineering Discovery Environment (XSEDE), which is supported by National Science Foundation grant number ACI-1548562, under allocation No. TG-DMR110091.

Supporting Information Available

The Supporting Information is available free of charge at DOI:

Details of the DP method and training procedure, equation of state calculation results for the Rogge *et al.* potential, influence of D3 corrections, velocity autocorrelation function decay, grand canonical Monte Carlo calculation details, comparison of xenon diameter to pore window size (PDF)

Sample input files (ZIP)

References

(1) Davis, M. E. Ordered Porous Materials for Emerging Applications. *Nature* **2002**, *417*, 813–821.

(2) Chen, B.; Eddaoudi, M.; Hyde, S.; O'Keeffe, M.; Yaghi, O. Interwoven Metal-Organic Framework on a Periodic Minimal Surface with Extra-Large Pores. *Science* **2001**, *291*, 1021–1023.

(3) Zhu, Q.-L.; Xu, Q. Metal–Organic Framework Composites. *Chem. Soc. Rev.* **2014**, *43*, 5468–5512.

(4) Lee, J.; Farha, O. K.; Roberts, J.; Scheidt, K. A.; Nguyen, S. T.; Hupp, J. T. Metal–Organic Framework Materials as Catalysts. *Chem. Soc. Rev.* **2009**, *38*, 1450–1459.

(5) Mandal, S.; Natarajan, S.; Mani, P.; Pankajakshan, A. Post-Synthetic Modification of Metal–Organic Frameworks Toward Applications. *Adv. Funct. Mater.* **2021**, *31*, 2006291.

(6) Martin, R. L.; Simon, C. M.; Smit, B.; Haranczyk, M. In silico Design of Porous Polymer Networks: High-Throughput Screening for Methane Storage Materials. *J. Am. Chem. Soc* **2014**, *136*, 5006–5022.

(7) Chung, Y. G.; Camp, J.; Haranczyk, M.; Sikora, B. J.; Bury, W.; Krungleviciute, V.; Yildirim, T.; Farha, O. K.; Sholl, D. S.; Snurr, R. Q. Computation-Ready, Experi-

mental Metal–Organic Frameworks: A Tool To Enable High-Throughput Screening of Nanoporous Crystals. *Chem. Mater.* **2014**, *26*, 6185–6192.

(8) Schroden, R. C.; Al-Daous, M.; Sokolov, S.; Melde, B. J.; Lytle, J. C.; Stein, A.; Carbajo, M. C.; Fernández, J. T.; Rodríguez, E. E. Hybrid Macroporous Materials for Heavy Metal Ion Adsorption. *J. Marwe. Chem.* **2002**, *12*, 3261–3267.

(9) James, S. L. Metal-Organic Frameworks. *Chem. Soc. Rev.* **2003**, *32*, 276–288.

(10) Stein, A. Advances in Microporous and Mesoporous Solids—Highlights of Recent Progress. *Adv. Mater.* **2003**, *15*, 763–775.

(11) García, H.; Navalón, S. *Metal-Organic Frameworks: Applications in Separations and Catalysis*; John Wiley & Sons, 2018.

(12) Shultz, A. M.; Farha, O. K.; Hupp, J. T.; Nguyen, S. T. A Catalytically Active, Permanently Microporous MOF with Metalloporphyrin Struts. *J. Am. Chem. Soc.* **2009**, *131*, 4204–4205.

(13) Nelson, A. P.; Farha, O. K.; Mulfort, K. L.; Hupp, J. T. Supercritical Processing as a Route to High Internal Surface Areas and Permanent Microporosity in Metal-Organic Framework Materials. *J. Am. Chem. Soc.* **2009**, *131*, 458–460.

(14) Demessence, A.; D'Alessandro, D. M.; Foo, M. L.; Long, J. R. Strong CO_2 Binding in a Water-Stable, Triazolate-Bridged Metal-Organic Framework Functionalized with Ethylenediamine. *J. Am. Chem. Soc.* **2009**, *131*, 8784–8786.

(15) Murray, L. J.; Dinca, M.; Yano, J.; Chavan, S.; Bordiga, S.; Brown, C. M.; Long, J. R. Highly-Selective and Reversible O2 Binding in Cr3 (1, 3, 5-benzenetricarboxylate)2. *J. Am. Chem. Soc.* **2010**, *132*, 7856–7857.

(16) Mulfort, K. L.; Farha, O. K.; Malliakas, C. D.; Kanatzidis, M. G.; Hupp, J. T. An

Interpenetrated Framework Material with Hysteretic CO_2 Uptake. *Chemistry* **2010**, *16*, 276–281.

(17) Savonnet, M.; Bazer-Bachi, D.; Bats, N.; Perez-Pellitero, J.; Jeanneau, E.; Lecocq, V.; Pinel, C.; Farrusseng, D. Generic Postfunctionalization Route from Amino-Derived Metal- Organic Frameworks. *J. Am. Chem. Soc.* **2010**, *132*, 4518–4519.

(18) Corma, A.; García, H.; Llabrés i Xamena, F. Engineering Metal Organic Frameworks for Heterogeneous Catalysis. *Chem. Rev.* **2010**, *110*, 4606–4655.

(19) Agrawal, M.; Boulfelfel, S. E.; Sava Gallis, D. F.; Greathouse, J. A.; Sholl, D. S. Determining Diffusion Coefficients of Chemical Warfare Agents in Metal–Organic Frameworks. *J. Phys. Chem. Lett.* **2019**, *10*, 7823–7830.

(20) Matito-Martos, I.; Moghadam, P. Z.; Li, A.; Colombo, V.; Navarro, J. A.; Calero, S.; Fairen-Jimenez, D. Discovery of an Optimal Porous Crystalline Material for the Capture of Chemical Warfare Agents. *Chem. Mater.* **2018**, *30*, 4571–4579.

(21) Zhao, J.; Lee, D. T.; Yaga, R. W.; Hall, M. G.; Barton, H. F.; Woodward, I. R.; Oldham, C. J.; Walls, H. J.; Peterson, G. W.; Parsons, G. N. Ultra-Fast Degradation of Chemical Warfare Agents Using MOF–Nanofiber Kebabs. *Angew. Chem.* **2016**, *128*, 13418–13422.

(22) Mondloch, J. E.; Katz, M. J.; Isley Iii, W. C.; Ghosh, P.; Liao, P.; Bury, W.; Wagner, G. W.; Hall, M. G.; DeCoste, J. B.; Peterson, G. W., et al. Destruction of Chemical Warfare Agents using Metal–Organic Frameworks. *Nat. Mater.* **2015**, *14*, 512–516.

(23) Gallis, D. F. S.; Harvey, J. A.; Pearce, C. J.; Hall, M. G.; DeCoste, J. B.; Kinnan, M. K.; Greathouse, J. A. Efficient MOF-Based Degradation of Organophosphorus Compounds in Non-Aqueous Environments. *J. Mater. Chem. A* **2018**, *6*, 3038–3045.

(24) Melnychuk, S. A.; Neverov, A. A.; Brown, R. S. Catalytic Decomposition of Simulants for Chemical Warfare V agents: Highly Efficient Catalysis of the Methanolysis of Phosphonothioate Esters. *Angew. Chem.* **2006**, *118*, 1799–1802.

(25) Moon, S.-Y.; Liu, Y.; Hupp, J. T.; Farha, O. K. Instantaneous Hydrolysis of Nerve-Agent Simulants with a Six-Connected Zirconium-Based Metal–Organic Framework. *Angew. Chem.* **2015**, *127*, 6899–6903.

(26) Wang, H.; Mahle, J. J.; Tovar, T. M.; Peterson, G. W.; Hall, M. G.; DeCoste, J. B.; Buchanan, J. H.; Karwacki, C. J. Solid-Phase Detoxification of Chemical Warfare Agents using Zirconium-Based Metal Organic Frameworks and the Moisture Effects: Analyze via Digestion. *ACS Appl. Mater. Interfaces* **2019**, *11*, 21109–21116.

(27) Ruffley, J. P.; Goodenough, I.; Luo, T.-Y.; Richard, M.; Borguet, E.; Rosi, N. L.; Johnson, J. K. Design, Synthesis, and Characterization of Metal–Organic Frameworks for Enhanced Sorption of Chemical Warfare Agent Simulants. *J. Phys. Chem. C* **2019**, *123*, 19748–19758.

(28) Kirlikovali, K. O.; Chen, Z.; Islamoglu, T.; Hupp, J. T.; Farha, O. K. Zirconium-based Metal–Organic Frameworks for the Catalytic Hydrolysis of Organophosphorus Nerve Agents. *ACS Appl. Mater. Interfaces* **2020**, *12*, 14702–14720.

(29) Son, F. A.; Wasson, M. C.; Islamoglu, T.; Chen, Z.; Gong, X.; Hanna, S. L.; Lyu, J.; Wang, X.; Idrees, K. B.; Mahle, J. J., et al. Uncovering the Role of Metal–Organic Framework Topology on the Capture and Reactivity of Chemical Warfare Agents. *Chem. Mater.* **2020**, *32*, 4609–4617.

(30) Liu, Y.; Howarth, A. J.; Vermeulen, N. A.; Moon, S.-Y.; Hupp, J. T.; Farha, O. K. Catalytic Degradation of Chemical Warfare Agents and their Simulants by Metal-Organic Frameworks. *Coord. Chem. Rev* **2017**, *346*, 101–111.

(31) Islamoglu, T.; Chen, Z.; Wasson, M. C.; Buru, C. T.; Kirlikovali, K. O.; Afrin, U.; Mian, M. R.; Farha, O. K. Metal–Organic Frameworks Against Toxic Chemicals. *Chem. Rev.* **2020**, *120*, 8130–8160.

(32) Wu, H.; Yildirim, T.; Zhou, W. Exceptional Mechanical Stability of Highly Porous Zirconium Metal–Organic Framework UiO-66 and Its Important Implications. *J. Phys. Chem. Lett.* **2013**, *4*, 925–930.

(33) Valenzano, L.; Civalleri, B.; Chavan, S.; Bordiga, S.; Nilsen, M. H.; Jakobsen, S.; Lillerud, K. P.; Lamberti, C. Disclosing the Complex Structure of UiO-66 Metal Organic Framework: A Synergic Combination of Experiment and Theory. *Chem. Mater.* **2011**, *23*, 1700–1718.

(34) Shearer, G. C.; Forselv, S.; Chavan, S.; Bordiga, S.; Mathisen, K.; Bjørgen, M.; Svelle, S.; Lillerud, K. P. In Situ Infrared Spectroscopic and Gravimetric Characterisation of the Solvent Removal and Dehydroxylation of the Metal Organic Frameworks UiO-66 and UiO-67. *Top. Catal.* **2013**, *56*, 770–782.

(35) Ryder, M. R.; Maul, J.; Civalleri, B.; Erba, A. Quasi-Harmonic Lattice Dynamics of a Prototypical Metal–Organic Framework. *Adv. Theory Simul.* **2019**, *2*, 1900093.

(36) Odoh, S. O.; Cramer, C. J.; Truhlar, D. G.; Gagliardi, L. Quantum-Chemical Characterization of the Properties and Reactivities of Metal–Organic Frameworks. *Chem. Rev.* **2015**, *115*, 6051–6111.

(37) Saiz, F.; Bernasconi, L. Electronic Structure and Reactivity of Fe (IV) Oxo Species in Metal–Organic Frameworks. *Phys. Chem. Chem. Phys.* **2019**, *21*, 4965–4974.

(38) Saiz, F.; Bernasconi, L. Density-Functional Theory Models of Fe (iv) O Reactivity in Metal–Organic Frameworks: Self-Interaction Error, Spin Delocalisation and the Role of Hybrid Exchange. *Phys. Chem. Chem. Phys.* **2020**, *22*, 12821–12830.

(39) Saiz, F.; Bernasconi, L. Unveiling the Catalytic Potential of the Fe (IV) oxo Species for the Oxidation of Hydrocarbons in the Solid State. *Catal. Sci. Technol.* **2021**,

(40) Lee, K.; Howe, J. D.; Lin, L.-C.; Smit, B.; Neaton, J. B. Small-Molecule Adsorption in Open-site metal–Organic Frameworks: A Systematic Density Functional Theory Study for Rational Design. *Chem. Mater.* **2015**, *27*, 668–678.

(41) Liu, Y.; Liu, H.; Hu, Y.; Jiang, J. Density Functional Theory for Adsorption of Gas Mixtures in Metal-Organic Frameworks. *J. Phys. Chem. B* **2010**, *114*, 2820–2827.

(42) Dubbeldam, D.; Walton, K. S.; Ellis, D. E.; Snurr, R. Q. Exceptional Negative Thermal Expansion in Isoreticular Metal–Organic Frameworks. *Angew. Chem.* **2007**, *119*, 4580–4583.

(43) Bristow, J. K.; Tiana, D.; Walsh, A. Transferable Force Field for Metal–Organic Frameworks from First-Principles: BTW-FF. *J. Chem. Theory Comput.* **2014**, *10*, 4644–4652.

(44) Addicoat, M. A.; Vankova, N.; Akter, I. F.; Heine, T. Extension of the Universal Force Field to Metal–Organic Frameworks. *J. Chem. Theory Comput.* **2014**, *10*, 880–891.

(45) Coupry, D. E.; Addicoat, M. A.; Heine, T. Extension of the Universal Force Field for Metal–Organic Frameworks. *J. Chem. Theory Comput.* **2016**, *12*, 5215–5225.

(46) Bureekaew, S.; Amirjalayer, S.; Tafipolsky, M.; Spickermann, C.; Roy, T. K.; Schmid, R. MOF-FF–A Flexible First-principles Derived Force Field for Metal-Organic Frameworks. *Phys. Status Solii B Basic Res.* **2013**, *250*, 1128–1141.

(47) Sun, Y.; Sun, H. An All-Atom Force Field Developed for $Zn_4O(RCO_2)_6$ Metal Organic Frameworks. *J. Mol. Model.* **2014**, *20*, 2146.

(48) Hu, Z.; Zhang, L.; Jiang, J. Development of a Force Field for Zeolitic Imidazolate Framework-8 with Structural Flexibility. *J. Chem. Phys.* **2012**, *136*, 244703.

(49) Tafipolsky, M.; Schmid, R. Systematic First Principles Parameterization of Force Fields for Metal-Organic Frameworks using a Genetic Algorithm Approach. *J. Phys. Chem. B* **2009**, *113*, 1341–1352.

(50) Zhao, L.; Yang, Q.; Ma, Q.; Zhong, C.; Mi, J.; Liu, D. A Force Field for Dynamic Cu-BTC Metal-Organic Framework. *J. Mol. Model.* **2011**, *17*, 227–234.

(51) Skoulidas, A. I. Molecular Dynamics Simulations of Gas Diffusion in Metal- Organic Frameworks: Argon in CuBTC. *J. Am. Chem. Soc.* **2004**, *126*, 1356–1357.

(52) Keskin, S. Gas Adsorption and Diffusion in a Highly CO_2 Selective Metal–Organic Framework: Molecular Simulations. *Mol. Simul.* **2013**, *39*, 14–24.

(53) Liu, B.; Yang, Q.; Xue, C.; Zhong, C.; Smit, B. Molecular Simulation of Hydrogen Diffusion in Interpenetrated Metal–Organic Frameworks. *Phys. Chem. Chem. Phys.* **2008**, *10*, 3244–3249.

(54) Parkes, M. V.; Demir, H.; Teich-McGoldrick, S. L.; Sholl, D. S.; Greathouse, J. A.; Allendorf, M. D. Molecular Dynamics Simulation of Framework Flexibility Effects on Noble Gas Diffusion in HKUST-1 and ZIF-8. *Microporous Mesoporous Mater.* **2014**, *194*, 190–199.

(55) Vargas L, E.; Snurr, R. Q. Heterogeneous Diffusion of Alkanes in the Hierarchical Metal–Organic Framework NU-1000. *Langmuir* **2015**, *31*, 10056–10065.

(56) Bigdeli, A.; Khorasheh, F.; Tourani, S.; Khoshgard, A.; Bidaroni, H. H. Molecular Simulation Study of the Adsorption and Diffusion Properties of Terephthalic Acid in Various Metal Organic Frameworks. *J. Inorg. Orgabomet. Polym. Matter.* **2020**, *30*, 1643–1652.

(57) Cabrales-Navarro, F. A.; Gómez-Ballesteros, J. L.; Balbuena, P. B. Molecular Dy-

namics Simulations of Metal-Organic Frameworks as Membranes for Gas Mixtures Separation. *J. Memb. Sci.* **2013**, *428*, 241–250.

(58) Verploegh, R. J.; Nair, S.; Sholl, D. S. Temperature and Loading-Dependent Diffusion of Light Hydrocarbons in ZIF-8 as Predicted Through Fully Flexible Molecular Simulations. *J. Am. Chem. Soc.* **2015**, *137*, 15760–15771.

(59) Farzi, N.; Salehi, N.; Mahboubi, A. Molecular Dynamics Simulation of Acetylene Diffusion in MOF-508a and MOF-508b. *Microporous Mesoporous Mater.* **2017**, *248*, 246–255.

(60) Hamon, L.; Llewellyn, P. L.; Devic, T.; Ghoufi, A.; Clet, G.; Guillerm, V.; Pirngruber, G. D.; Maurin, G.; Serre, C.; Driver, G.; van Beek, W.; Jolimaître, E.; Vimont, A.; Daturi, M.; Férey, G. Co-adsorption and Separation of CO_2-CH_4 Mixtures in the Highly Flexible MIL-53(Cr) MOF. *J. Am. Chem. Soc.* **2009**, *131*, 17490–17499.

(61) Han, C.; Yang, Y.; Sholl, D. S. Quantitatively Predicting Impact of Structural Flexibility on Molecular Diffusion in Small Pore Metal–Organic Frameworks—A Molecular Dynamics Study of Hypothetical ZIF-8 Polymorphs. *J. Phys. Chem. C* **2020**, *124*, 20203–20212.

(62) Yang, Y.; Sholl, D. S. A systematic examination of the impacts of MOF flexibility on intracrystalline molecular diffusivities. *J. Mater. Chem. A* **2022**, *10*, 4242–4253.

(63) Wardzala, J. J.; Ruffley, J. P.; Goodenough, I.; Schmidt, A. M.; Shukla, P. B.; Wei, X.; Bagusetty, A.; De Souza, M.; Das, P.; Thompson, D. J., et al. Modeling of Diffusion of Acetone in UiO-66. *J. Phys. Chem. C* **2020**,

(64) Yang, Q.; Jobic, H.; Salles, F.; Kolokolov, D.; Guillerm, V.; Serre, C.; Maurin, G. Probing the Dynamics of CO_2 and CH_4 within the Porous Zirconium Terephthalate UiO-66(Zr): A Synergic Combination of Neutron Scattering Measurements and Molecular Simulations. *Chemistry* **2011**, *17*, 8882–8889.

(65) Seehamart, K.; Nanok, T.; Kärger, J.; Chmelik, C.; Krishna, R.; Fritzsche, S. Investigating the Reasons for the Significant Influence of Lattice Flexibility on Self-Diffusivity of Ethane in Zn(Tbip). *Microporous and Mesoporous Mater.* **2010**, *130*, 92–96.

(66) Zhang, L.; Wu, G.; Jiang, J. Adsorption and Diffusion of CO_2 and CH_4 in Zeolitic Imidazolate Framework-8: Effect of Structural Flexibility. *J. Phys. Chem. C* **2014**, *118*, 8788–8794.

(67) Vanduyfhuys, L.; Vandenbrande, S.; Verstraelen, T.; Schmid, R.; Waroquier, M.; Van Speybroeck, V. QuickFF: A program for a quick and easy derivation of force fields for metal-organic frameworks from ab initio input. *J. Comput. Chem.* **2015**, *36*, 1015–1027.

(68) Vanduyfhuys, L.; Vandenbrande, S.; Wieme, J.; Waroquier, M.; Verstraelen, T.; Van Speybroeck, V. Extension of the QuickFF Force Field Protocol for an Improved Accuracy of Structural, Vibrational, Mechanical and Thermal Properties of Metal–Organic Frameworks. *J. Comput. Chem.* **2018**, *39*, 999–1011.

(69) Dürholt, J. P.; Fraux, G.; Coudert, F.-X.; Schmid, R. Ab Initio Derived Force Fields for Zeolitic Imidazolate Frameworks: MOF-FF for ZIFs. *J. Chem. Theory Comput.* **2019**, *15*, 2420–2432, PMID: 30865448.

(70) Weng, T.; Schmidt, J. R. Flexible and Transferable ab Initio Force Field for Zeolitic Imidazolate Frameworks: ZIF-FF. *J. Phys. Chem. A* **2019**, *123*, 3000–3012.

(71) Popelier, P. L. A.; Aicken, F.; O'Brien, S. *Atoms In Molecules*; Prentice Hall Manchester, 2000.

(72) Rappé, A. K.; Casewit, C. J.; Colwell, K.; Goddard III, W. A.; Skiff, W. M. UFF, a Full Periodic Table Force Field for Molecular Mechanics and Molecular Dynamics Simulations. *J. Am. Chem. Soc.* **1992**, *114*, 10024–10035.

(73) Zhang, X.; Zhang, K.; Lee, Y. Machine Learning Enabled Tailor-Made Design of Application-Specific Metal–Organic Frameworks. *ACS Appl. Mater. Interfaces* **2019**, *12*, 734–743.

(74) Moghadam, P. Z.; Rogge, S. M.; Li, A.; Chow, C.-M.; Wieme, J.; Moharrami, N.; Aragones-Anglada, M.; Conduit, G.; Gomez-Gualdron, D. A.; Van Speybroeck, V., et al. Structure-Mechanical Stability Relations of Metal-Organic Frameworks via Machine Learning. *Matter* **2019**, *1*, 219–234.

(75) Shi, Z.; Yang, W.; Deng, X.; Cai, C.; Yan, Y.; Liang, H.; Liu, Z.; Qiao, Z. Machine-Learning-Assisted High-Throughput Computational Screening of High Performance Metal–Organic Frameworks. *Mol. Syst. Des. Eng.* **2020**, *5*, 725–742.

(76) Chong, S.; Lee, S.; Kim, B.; Kim, J. Applications of Machine Learning in Metal-Organic Frameworks. *Coord. Chem. Rev.* **2020**, *423*, 213487.

(77) Gurnani, R.; Yu, Z.; Kim, C.; Sholl, D. S.; Ramprasad, R. Interpretable Machine Learning-Based Predictions of Methane Uptake Isotherms in Metal–Organic Frameworks. *Chemistry of Materials* **2021**, *33*, 3543–3552.

(78) Eckhoff, M.; Behler, J. From Molecular Fragments to the Bulk: Development of a Neural Network Potential for MOF-5. *J. Chem. Theory Comput.* **2019**, *15*, 3793–3809.

(79) Behler, J.; Parrinello, M. Generalized Neural-Network Representation of High-Dimensional Potential-Energy Surfaces. *Phys. Rev. Lett.* **2007**, *98*, 146401.

(80) Schütt, K. T.; Arbabzadah, F.; Chmiela, S.; Müller, K. R.; Tkatchenko, A. Quantum-Chemical Insights from Deep Tensor Neural Networks. *Nat. Commun.* **2017**, *8*, 1–8.

(81) Yao, K.; Herr, J. E.; Brown, S. N.; Parkhill, J. Intrinsic Bond Energies from a Bonds-in-Molecules Neural Network. *J. Phys. Chem. Lett.* **2017**, *8*, 2689–2694.

(82) Chmiela, S.; Tkatchenko, A.; Sauceda, H. E.; Poltavsky, I.; Schütt, K. T.; Müller, K.-R. Machine Learning of Accurate Energy-Conserving Molecular Force Fields. *Science advances* **2017**, *3*, e1603015.

(83) Zhang, L.; Han, J.; Wang, H.; Car, R.; E, W. Deep Potential Molecular Dynamics: A Scalable Model with the Accuracy of Quantum Mechanics. *Phys. Rev. Lett.* **2018**, *120*, 143001.

(84) Zhang, L.; Han, J.; Wang, H.; Saidi, W.; Car, R.; E, W. End-to-end Symmetry Preserving Inter-atomic Potential Energy Model for Finite and Extended Systems. Advances in Neural Information Processing Systems. 2018; pp 4441–4451.

(85) Wang, H.; Zhang, L.; Han, J.; E, W. DeePMD-kit:A Deep Learning Package for Many-Body Potential Energy Representation and Molecular Dynamics. *Comput. Phys. Commun.* **2018**, *228*, 178–184.

(86) Plimpton, S. Fast Parallel Algorithms for Short-Range Molecular Dynamics. *J. Comput. Phys.* **1995**, *117*, 1–19.

(87) Larsen, A. H.; Mortensen, J. J.; Blomqvist, J.; Castelli, I. E.; Christensen, R.; Dułak, M.; Friis, J.; Groves, M. N.; Hammer, B.; Hargus, C., et al. Atomic Simulation Environment—a Python Library for Working with Atoms. *J. Phys. Condens. Matter* **2017**, *29*, 273002.

(88) Rogge, S. M.; Wieme, J.; Vanduyfhuys, L.; Vandenbrande, S.; Maurin, G.; Verstraelen, T.; Waroquier, M.; Van Speybroeck, V. Thermodynamic Insight in the High-Pressure Behavior of UiO-66: Effect of Linker Defects and Linker Expansion. *Chem. Mater.* **2016**, *28*, 5721–5732.

(89) Guevara-Carrion, G.; Hasse, H.; Vrabec, J. In *Multiscale Molecular Methods in Applied Chemistry*; Kirchner, B and Vrabec, J,, Ed.; Topics in Current Chemistry-Series; 2012; Vol. 307; pp 201–249.

(90) Eggimann, B. L.; Sunnarborg, A. J.; Stern, H. D.; Bliss, A. P.; Siepmann, J. I. An Online Parameter and Property Database for the TraPPE Force Field. *Mol. Simul.* **2014**, *40*, 101–105.

(91) Ferrando, N.; Lachet, V.; Teuler, J.-M.; Boutin, A. Transferable Force Field for Alcohols and Polyalcohols. *J. Phys. Chem. B* **2009**, *113*, 5985–5995, PMID: 19344171.

(92) Sakae, Y.; Okamoto, Y. Optimisation of OPLS–UA Force-Field Parameters for Protein Systems Using Protein Data Bank. *Mol. Simul.* **2010**, *36*, 1148–1156.

(93) Mayo, S. L.; Olafson, B. D.; Goddard, W. A. DREIDING: a Generic Force Field for Molecular Simulations. *J. Phys. Chem.* **1990**, *94*, 8897–8909.

(94) Haldoupis, E.; Watanabe, T.; Nair, S.; Sholl, D. S. Quantifying Large Effects of Framework Flexibility on Diffusion in MOFs: CH4 and CO2 in ZIF-8. *ChemPhysChem* **2012**, *13*, 3449–3452.

(95) Achar, S. K.; Zhang, L.; Johnson, J. K. Efficiently Trained Deep Learning Potential for Graphane. *J. Phys. Chem. C* **2021**,

(96) Øien, S.; Wragg, D.; Reinsch, H.; Svelle, S.; Bordiga, S.; Lamberti, C.; Lillerud, K. P. Detailed Structure Analysis of Atomic Positions and Defects in Zirconium Metal–Organic Frameworks. *Cryst. Growth Des.* **2014**, *14*, 5370–5372.

(97) Zhu, L.; Zhang, D.; Xue, M.; Li, H.; Qiu, S. Direct Observations of the MOF (UiO-66) Structure by Transmission Electron Microscopy. *CrystEngComm* **2013**, *15*, 9356–9359.

(98) Kresse, G.; Hafner, J. Ab Initio Molecular Dynamics for Liquid Metals. *Phys. Rev. B* **1993**, *47*, 558–561.

(99) Kresse, G.; Hafner, J. Ab Initio Molecular-Dynamics Simulation of the Liquid-Metal–Amorphous-Semiconductor Transition in Germanium. *Phys. Rev. B* **1994**, *49*, 14251–14269.

(100) Kresse, G.; Furthmüller, J. Efficiency of Ab-Initio Total Energy Calculations for Metals and Semiconductors Using a Plane-Wave Basis Set. *Comput. Mater. Sci.* **1996**, *6*, 15–50.

(101) Kresse, G.; Furthmüller, J. Efficient Iterative Schemes for Ab Initio Total-Energy Calculations Using a Plane-Wave Basis Set. *Phys. Rev. B* **1996**, *54*, 11169.

(102) Blöchl, P. E. Projector Augmented-Wave Method. *Phys. Rev. B* **1994**, *50*, 17953.

(103) Perdew, J. P.; Burke, K.; Ernzerhof, M. Generalized Gradient Approximation Made Simple. *Phys. Rev. Lett.* **1996**, *77*, 3865.

(104) Zhang, Y.; Yang, W. Comment on "Generalized Gradient Approximation Made Simple". *Phys. Rev. Lett.* **1998**, *80*, 890.

(105) Evans, D. J.; Holian, B. L. The Nose–Hoover Thermostat. *J. Chem. Phys.* **1985**, *83*, 4069–4074.

(106) Deepmodeling, deepmodeling/deepmd-kit. https://github.com/deepmodeling/deepmd-kit, `https://github.com/deepmodeling/deepmd-kit`.

(107) Zhang, Y.; Wang, H.; Chen, W.; Zeng, J.; Zhang, L.; Wang, H.; Weinan, E. DP-GEN: A Concurrent Learning Platform for the Generation of Reliable Deep Learning Based Potential Energy Models. *Comput. Phys. Commun.* **2020**, *253*, 107206.

(108) Verstraelen, T.; Vandenbrande, S.; Heidar-Zadeh, F.; Vanduyfhuys, L.; Van Speybroeck, V.; Waroquier, M.; Ayers, P. W. Minimal Basis Iterative Stockholder: Atoms in Molecules for Force-Field Development. *J. Chem. Theory Comput.* **2016**, *12*, 3894–3912.

(109) Boyd, P. G.; Moosavi, S. M.; Witman, M.; Smit, B. Force-field prediction of materials properties in metal-organic frameworks. *J. Phys. Chem. Lett.* **2017**, *8*, 357–363.

(110) Birch, F. Finite Elastic Strain of Cubic Crystals. *Phys. Rev.* **1947**, *71*, 809.

(111) Murnaghan, F. The Compressibility of Media Under Extreme Pressures. *Proc. Natl. Acad. Sci. U.S.A.* **1944**, *30*, 244.

(112) Redfern, L. R.; Robison, L.; Wasson, M. C.; Goswami, S.; Lyu, J.; Islamoglu, T.; Chapman, K. W.; Farha, O. K. Porosity Dependence of Compression and Lattice Rigidity in Metal–Organic Framework Series. *J. Am. Chem. Soc.* **2019**, *141*, 4365–4371.

(113) Becke, A. D. Density-Functional Exchange-Energy Approximation with Correct Asymptotic Behavior. *Phys. Rev. A* **1988**, *38*, 3098.

(114) Vosko, S. H.; Wilk, L.; Nusair, M. Accurate Spin-Dependent Electron Liquid Correlation Energies for Local Spin Density Calculations: a Critical Analysis. *Can. J. Phys.* **1980**, *58*, 1200–1211.

(115) Frisch, M.; Trucks, G.; Schlegel, H.; Scuseria, G.; Robb, M.; Cheeseman, J.; Scalmani, G.; Barone, V.; Mennucci, B.; Petersson, G., et al. Gaussian 09, Revision D. 01, 2009, Gaussian. *Inc., Wallingford CT* **2009**,

(116) Cavka, J. H.; Jakobsen, S.; Olsbye, U.; Guillou, N.; Lamberti, C.; Bordiga, S.; Lillerud, K. P. A New Zirconium Inorganic Building Brick Forming Metal Organic Frameworks with Exceptional Stability. *J. Am. Chem. Soc.* **2008**, *130*, 13850–13851.

(117) Grimme, S.; Ehrlich, S.; Goerigk, L. Effect of the Damping Function in Dispersion Corrected Density Functional Theory. *J. Comput. Chem.* **2011**, *32*, 1456–1465.

(118) Morales, J. J.; Nuevo, M. J. Path Integral Molecular Dynamics Methods: Application to Neon. *J. Comput. Chem.* **1995**, *16*, 105–112.

(119) Simonyan, V. V.; Johnson, J. K.; Kuznetsova, A.; Yates, J. T. Molecular simulation of

xenon adsorption on single-walled carbon nanotubes. *The Journal of Chemical Physics* **2001**, *114*, 4180–4185.

(120) Dubbeldam, D.; Calero, S.; Ellis, D. E.; Snurr, R. Q. RASPA: Molecular Simulation Software for Adsorption and Diffusion in Flexible Nanoporous Materials. *Mol. Simul.* **2016**, *42*, 81–101.

(121) Andersen, H. C. Molecular Dynamics Simulations at Constant Pressure and/or Temperature. *J. Chem. Phys.* **1980**, *72*, 2384–2393.

TOC Graphic

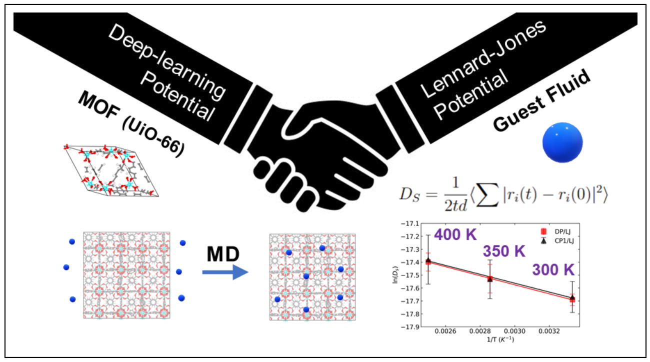
Deep-learning Potential
MOF (UiO-66)
Lennard-Jones Potential
Guest Fluid
$D_S = \frac{1}{2td}\langle \sum |r_i(t) - r_i(0)|^2 \rangle$
MD
400 K
350 K
300 K